Journal of Physics D:
Applied Physics

The effect of bending angle on a flexible electrode DBD plasma under sinusoidal excitation

To cite this article: Jiayin Li *et al* 2024 *J. Phys. D: Appl. Phys.* **57** 395201

OPEN ACCESS
IOP Publishing
Journal of Physics D: Applied Physics
J. Phys. D: Appl. Phys. **57** (2024) 395201 (14pp)
https://doi.org/10.1088/1361-6463/ad58ee

The effect of bending angle on a flexible electrode DBD plasma under sinusoidal excitation

Jiayin Li[1], **Desheng Zhou**[2], **Evgeny Rebrov**[3,4], **Xin Tang**[1] **and Minkwan Kim**[1,*]

[1] School of Engineering, University of Southampton, Southampton SO17 1BJ, United Kingdom
[2] School of Energy Science and Engineering, Harbin Institute of Technology, Heilongjiang, Harbin 150006, People's Republic of China
[3] School of Engineering, University of Warwick, Coventry CV4 7AL, United Kingdom
[4] Department of Chemical Engineering and Chemistry, Eindhoven University of Technology, PO Box 513, 5600 MB Eindhoven, The Netherlands

E-mail: m.k.kim@soton.ac.uk

Received 30 November 2023, revised 4 June 2024
Accepted for publication 17 June 2024
Published 5 July 2024

Abstract

There is a critical demand for sophisticated surface disinfection and sterilization devices accessible to the public by using cold atmospheric pressure air plasmas. A flexible printed circuit design of a dielectric barrier discharge reactor under non-bending and two bending configurations with an angle of 120° and 180° was studied. The characteristics of power consumption, the optical emission spectrum, dynamic process, electrode temperature and ozone concentration are evaluated. The non-bending configuration produces more O_3, as compared to the bending configuration at the same applied voltage. The 180° configuration has a maximum concentration of excited species at the expense of higher electrode temperature. Both bending configurations demonstrated the propagation of filaments to bending axis where the continues luminescence is observed due to the high electrical field. The energy efficiency for plasma-generated reactive species reaches to 40% for non-bending configuration and decreases with the increase of bending angle. This research provides a new strategy for perspective into the plasma generated reactive species in biomedical and environmental applications.

Keywords: surface dielectric barrier discharge, bending angle, ozone production, excited species, power dissipation

1. Introduction

Cold atmospheric pressure air plasmas (CAAPs) have drawn considerable interest in environmental and biomedical applications, where plasma-generated reactive species are considered to be the crucial constituents [1–3]. For instance, O_3 is a strong oxidant extensively utilized in water treatment [4–6] and disinfection [7, 8]. Over the last two decades, the CAAPs plasma sources are mainly focus on a floating electrode dielectric barrier discharge (FE-DBD) [9, 10], cold atmospheric pressure air plasma jets (CAAP-Js) [11, 12] and a less common surface DBD (SDBD) [13, 14]. In a FE-DBD device, the plasma is generated in the gap between the high voltage enclosed in a dielectric material and the treated surface severed as the ground electrode. The most extensively studied is the CAAP-Js, which is driven from dc power with a high voltage electrode often made by stainless steel needle. The air plasma effluent is user-friendly and easy-assemble but limited for the small area for processing and non-uniform discharge [12]. A

---

[*] Author to whom any correspondence should be addressed.

SDBD is composed of two electrodes positioned asymmetrically across a dielectric barrier, which generates a plasma above the barrier surface from the surrounding gas. It has been primarily studied as an actuator for regulating flow control in aeronautics and environmental applications due to the advantages of low-cost, uniform discharge and large-area surface processing [15, 16].

However, printed electronics technology, a novel method for fabricating electric circuits on a flexible board with metallic inks, facilitated its applications in the fields of complex surface processing [17–20]. For the application in disinfection of curved surface, Weltmann *et al* [21] introduced an flexible electrode array configuration suitable for intricate 3D geometries treatment. Liu *et al* [22] also reported a versatile multi-pin plasma generator featuring movable electrodes, enabling the uniform treatment of large surface areas with complex shapes. Kim *et al* [23] demonstrated an inkjet-printed flexible DBD (flex-DBD) source to inactivate the fungi on the surface of blueberries by decreasing the corruption rate of 80% for at least 5 min treatment. Gershman *et al* [19] investigated the surface decontamination from bacterial contaminants by combining a flex-DBD design with H_2O_2, achieving a remarkable six-log reduction in bacterial load on surfaces within 90 s. Recently, Guo *et al* [24] proposed a flexible plasma film based on SDBD, which could significantly reduce the pathogens on the film surface with the inhibition rate of 99.3% on the pseudovirus and killing rate of 94.3% on the natural bacteria.

The previous results demonstrated that flexible electrodes could conform to curved surfaces, realizing high decontamination and sterilization efficiency by reactive species. In general, when the electrical power is fed in the plasma, it produce reactive species (e.g. excited species and ozone) while also heating the electrode [25]. The parameters of the plasma are influenced by the discharge geometry and profound knowledge about the dissipated power. Different curved electrode configurations may provide different energy efficiency, which in turn, reflecting on the different power distribution. There may exist an optimum bending angle for achieving higher reactive species concentration without a significant increase in electrode temperature [10]. On the other hand, bending geometries may also alert the equivalent impedance of flex-DBD. However, so far, few studies focus on the power regulation and equivalent circuit analysis on bended electrode flex-DBD plasma.

In this paper, the characteristics including optical emission density, electrode temperature and ozone concentration of a flexible-SDBD at different bending angles, applied power were studied. The results will obtain further insights in the underlying mechanisms of plasma-generated reactive species and serve as a useful reference to inform environmental and biomedical applications.

2. Experimental setup

The schematic of the experimental setup is shown in figure 1. A porous SDBD plasma source based on a printed circuit design [18, 20]. Both the high voltage and ground electrode are printed on a dielectric substrate by conductive ink, arranged in an overlapping hexagonal pattern. An orifice with a 0.35 mm diameter is drilled into the SDBD plasma source. More details are provided in our previous work [15]. Three bending angles of 0°, 120° and 180° with a fixed bend radius were studied corresponding to a distance between the two electrode parts of infinity, 13 and 3 mm, respectively. They are shown in figures 2(b)–(d). For convenience, the flex-SDBD with a bending angle of 0°, 120° and 180° operation will further be referred to as the 0°, 120° and 180° configuration, respectively. The same electrode cell was used for all three configurations.

The flex-SDBD plasma source was powered by an AC high voltage source, created from a sinusoidal waveform signal by a signal generator (AFG1062, Tektronix), and an audio power amplifier (CDi DriveCore 2I600, Crown). The frequency of the ac power supply was fixed at 5 kHz. The peak-to-peak voltage of sinusoidal high voltage was varied from 4.6 to 6.0 kV. The electrical characteristics of the flex-SDBD plasma sources are detected by using a high voltage probe (P6015A, Tektronix) for the applied voltage and a Rogowski coil (Model 6585, Pearson Electronics) for the current, respectively. A 33 nF sampling capacitor (C_0) was placed in the electrical circuit to measure the transferred charge Q. Then the power consumption was calculated as the area of the Lissajous plot through equation (1) where f is the frequency, and V is the voltage [26]:

$$P = \frac{1}{f}\int Q\mathrm{d}V. \tag{1}$$

The plasma images were recorded with a digital single-lens reflex camera (Nikon D5600, AS-F Micro NIKKOR 40 mm). The dynamic images were taken by an ICCD camera (DH334T, Andor. Exposure time: 0.5 s, gain: 4000, width: 1 μs, increments: 15 μs). The trigger moments were at the trans-zero point where the sinewave voltage changes from positive to negative. The electrode surface temperature was measured with an IR-camera (C2, FLIR, emissivity $\varepsilon = 0.95$). Optical emission spectra were recorded with a spectrometer (Andor Shamrock SR500i, grating: 1800 groove mm^{-1}, slit width: 50 μm, step and glue mode) coupled with an Andor sCMOS. The spectra were collected at 5 mm away from the flex-SDBD reactor. A cosine corrector was coupled to optical fibers to collect all light within a 180° solid angle, suitable for measuring the light intensity from a planar surface or light from multiple surfaces [27]. The ozone concentration was measured by a gas analyzer (49iQ, Thermo Fisher Scientific).

The measurement of ozone, electrode temperature and optical spectrum depends on the positioning angle. Therefore, the data from top and side views were collected separately. It was assumed the side electrodes are symmetrical relative to the bending axis. Therefore, the intensity taken from side view was multiplied by 2 and added up with that taken from the top view. Then the sum was divided by 3. Prior to experiments, a 2 min plasma discharge was ignited to provide stable conditions. Each measurement was repeated three times at room temperature.

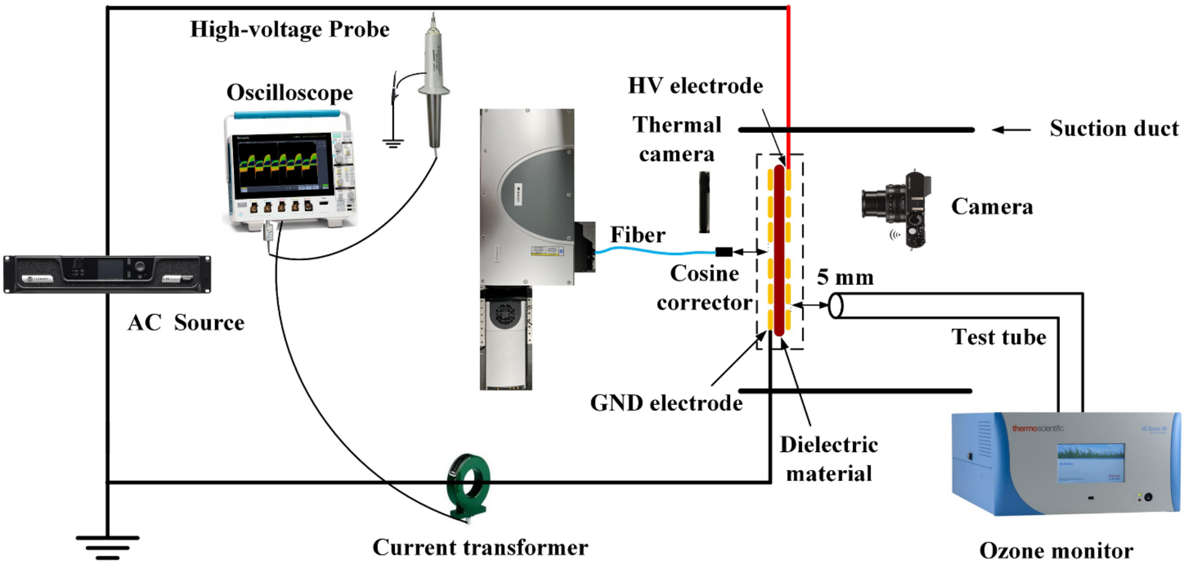

Figure 1. Schematic of the experimental setup.

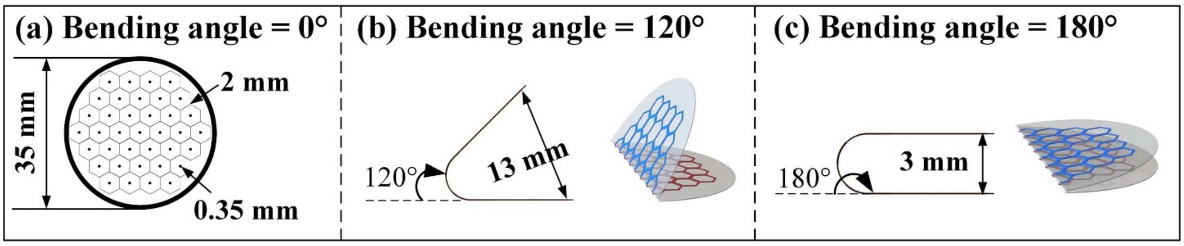

Figure 2. Porous surface DBD plasma source with 0° (a), 120° (b) and 180° configuration (c).

3. Results

3.1. Discharge images

Figure 3 shows plasma images for the three plasma configurations at an applied voltage of 4.8 and 5.4 kV. The electrode has many dark blue areas showing the discharge was incomplete at 4.8 kV for the 0° case. The discharge was enhanced and more purple areas were seen for the 120° and 180° configurations. From the top view, the discharge intensity of the 180° configuration was higher than that of the 120° configuration. However, a rather large dark area (no discharge) was seen in the side view for the 180° configuration, while the 120° configuration provided a more uniform plasma field. At a voltage of 5.4 kV, a greater part of the flex-DBD lights up. The plasma was more uniform and there were no dark blue areas in the images. The 180° configuration demonstrated a similar trend of discharge intensity with an area of low intensity clearly seen in the top view. The white color in both bending configurations suggested that the discharge intensity was much higher in that area [28]. By analyzing the image brightness and spatial distribution status, the distribution of discharge images is shown in figure 4 for the two voltages of 4.8 and 5.4 kV for the three configurations studied. It can be seen that for the 0° configuration, the intensity of discharge is higher at 5.4 kV than at 4.8 kV. Also, higher voltage results in a more uniform distribution of discharges. The intensity increases with increasing the bending angle.

3.2. Electrical characteristic

The U-I waveforms under different applied voltages are shown in figure 5. There were two breakdowns in each cycle, each occurring over every half cycle. The smallest discharge current was observed at 4.8 kV for the 0° configuration. The number and the amplitude of micro discharges in a single current pulse increased in the 120° configuration and further in the 180° configuration, as shown in table 1. An increase voltage of the discharge gap at higher bending angles leads to a higher number of micro discharges [29]. However, there is minor difference in the mean amplitude of micro discharge between non-bending and bending configurations. The 180° configuration resulted in the most intense discharge behavior with mean amplitude of 11.7 mA versus 10.5 mA in the 0° configuration. The greater number of micro discharges is responsible for a larger total charge transferred in the circuit.

Figure 6(a) shows the power consumption increases proportionally to the applied voltage for the three configurations. A maximum power consumption of 2.5 W was observed in the

Figure 3. Discharge images under different curved electrode conditions when the applied voltage was fixed at (a) $U_{p-p} = 4.8$ kV and (b) $U_{p-p} = 5.4$ kV (exposure time 1 s, ISO 3200, f/6.3).

180° configuration in figure 6(b). The basic power consumption in SDBD is very low, due to the reduced discharge distance between the electrodes ($\sim$10 μm rather than $\sim$1 mm), requiring a lower breakdown voltage based off the Paschen curve relationship [30]. However, the high intensity discharge area near the bending axis is relatively small as compared to the total discharge area in the bending configuration. Thus, there is minor difference in the power consumption between non-bending and bending configurations.

3.3. Optical emission

Figures 7 and 8 show optical emission spectra of flex-SDBD plasma at 4.8 and 5.4 kV measured from the top and from the side. The spectra revealed the presence of the molecular nitrogen $N_2(C^3\Pi_u$ CtB$^3\Pi_g)$, its secondary diffraction as well as the molecular nitrogen ion rotational bands $N_2^+(B^2\Sigma_u$ BiX$^2\Sigma_g)$ due to the high nitrogen content in the air. In each spectrum, $N_2(C^3\Pi_u$ CuB$^3\Pi_g)$ exhibited the highest emission intensity, followed by its secondary diffraction, while $N_2^+(B^2\Sigma_u$ BxX$^2\Sigma_g)$ displayed the lowest emission intensity.

Figure 9 shows the effect of the bending angles on the intensity of the emission spectrum of different bands from the top and from the side. With the increase of the bending angles, the emission intensity of all bands from the top view increased while the emission intensity of all bands from the side view decreased. The highest intensity of excited states was observed at 5.4 kV. In line with discharge images, the top view for the 180° configuration and the side view for the 120° configuration demonstrated the highest intensity. The intensity of all bands decreased at 4.8 kV. This is easy to understand since higher intensity of discharge results in a higher emission intensity [28]. No emission lines of O, OH, and hydrogen atoms were observed due to low concentration of H_2O in the air. These results are in line with the work by Wang *et al* [31].

3.4. Dynamic process

Figures 10 and 11 show the spatiotemporal images of the flex-SDBD plasma in a single discharge at 4.8 and 5.4 kV from the top and side view, respectively. The numbers in the scale bar (0–6000) represent the relative intensity of the color bar, which is proportional to the relative luminous intensity of the plasma. The plasma is produced in both positive and negative half cycles [28]. The maximum of light emission is reached at a time of 42 μs. The highest light intensity was observed for

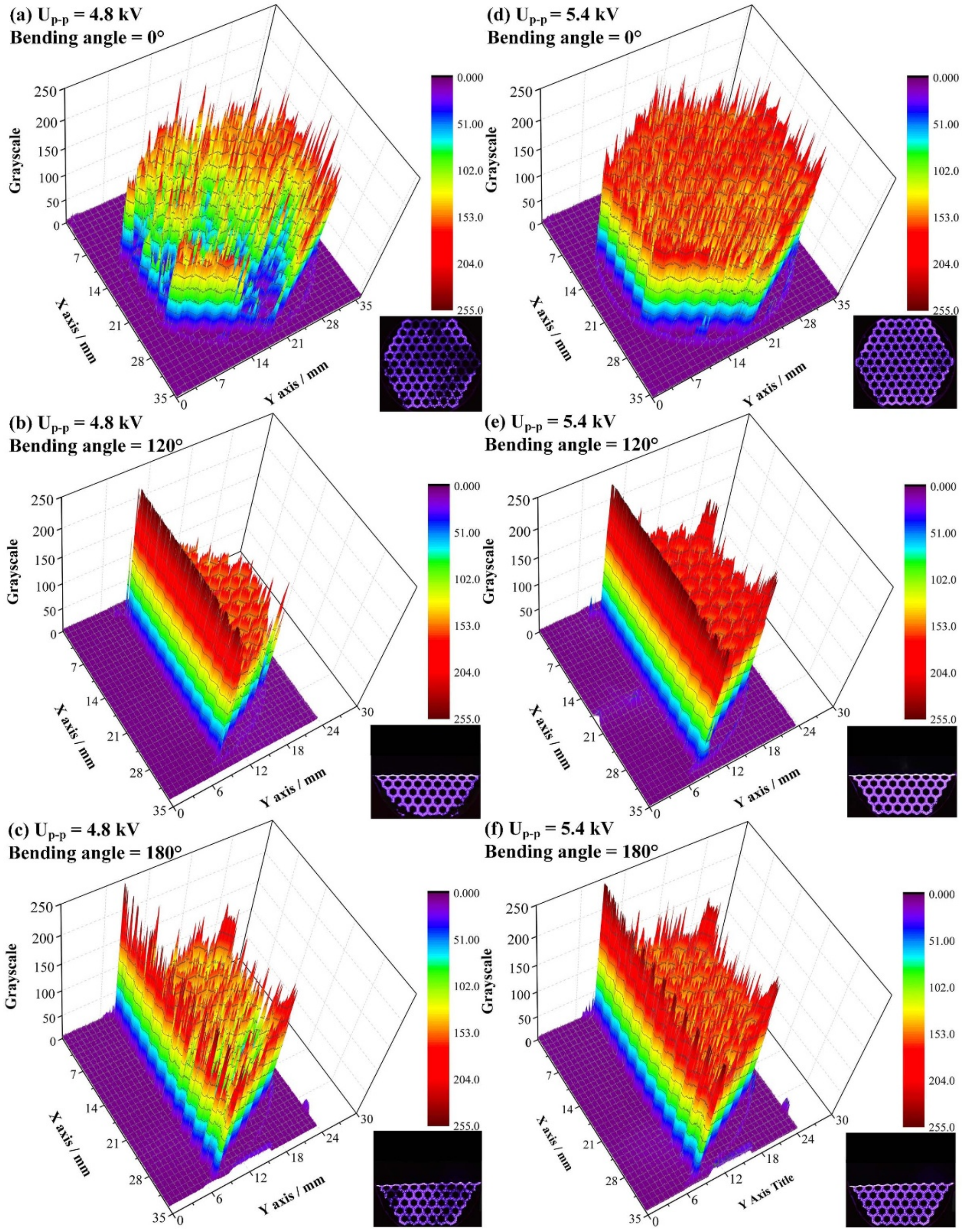

Figure 4. Distribution of discharge images from side view when the applied voltage was fixed at $U_{p-p} = 4.8$ kV: (a) 0°, (b) 120°, (c) 180° configuration and $U_{p-p} = 5.4$ kV: (d), 0°, (e) 120°, (f) 180° configuration.

the 120° and 180° configurations from the top view. First, the discharge occurs near the center of the electrode and then at the periphery (i.e. near the bending axis) when watching from the top view. When watching from the side view, it can be seen in figure 10 that the discharge starts from the right corner, due to the enhancement of the electric field. In the negative half cycle, the discharge remains at the bending position longer than that in the positive half cycle.

No essential differences were observed at the bending axis between the 120° and 180° configurations because the field strength was much higher than the breakdown field strength for air plasma. Therefore, the mean light intensity in one discharge cycle is listed in table 2 for the three configurations. The highest light intensity for the 180° configuration was observed at the top, while for the 120° configuration was observed from the side.

3.5. Electrode temperature and O_3 concentration

Figure 12 shows electrode temperature maps taken after 60 s from the top and side positions at two voltages of 4.8 and 5.4 kV. A temperature gradient was observed in both cases. The highest temperatures of 60.7 °C and 61.6 °C were recorded for the 180° configuration from the top and side view,

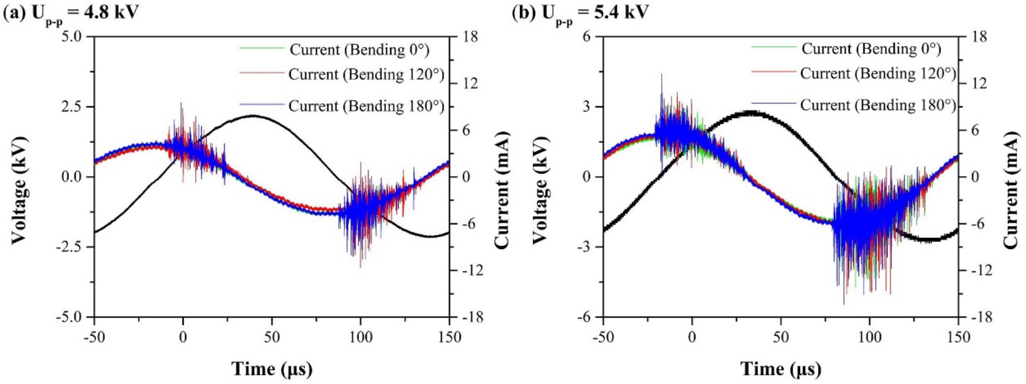

Figure 5. Discharge current and voltage waveforms. The current waveforms were marked green, blue and red line corresponding with 0°, 120° and 180° configurations, respectively.

Table 1. Number of micro discharges and their mean amplitude value for non-bending and bending configurations.

		Number of micro discharges		Mean amplitude of micro discharge	
Operation & configuration		Pos. period	Neg. period	Pos. period (mA)	Neg. period (mA)
$U_{p-p} = 4.8$ kV	0°	6	8	5.6	−7.4
	120°	10	15	6.3	−8.1
	180°	12	16	6.7	−8.5
$U_{p-p} = 5.4$ kV	0°	11	21	8.1	−10.5
	120°	13	24	8.5	−11.4
	180°	17	27	8.8	−11.7

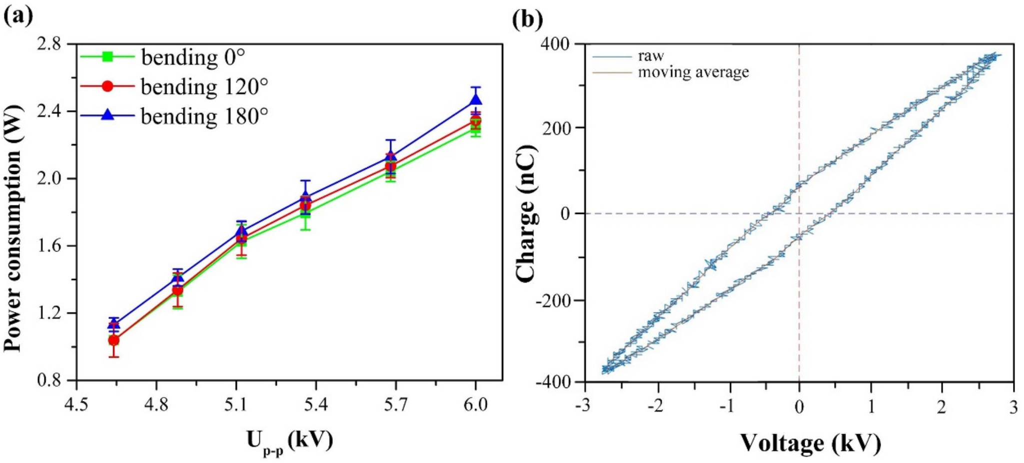

Figure 6. (a) Power consumption of flex-SDBD under different curved electrode conditions; (b) Lissajous plots for one full cycle of the sinusoidal applied voltage at 6 kV for 180° configuration.

respectively. The lowest temperature was recorded for the 0° configuration. It can be seen in figure 13(a) that the mean temperature increases with applied voltage due to higher heat generation rate by plasma. The temperature measured from the side was always by 2 K higher than that from the top. This is due to reduced radiative heat losses in the side view as the two parts of electrode are close to each other and therefore they lack participating in radiative heat exchange.

The O_3 concentration monotonously rises from 300 to about 700 ppb when the voltage increases from 4.6 to 5.7 kV for all three configurations (figure 13(b)). However, there is a sharp increase in electrode temperature to 76 °C and a decrease in O_3 concentration above 5.7 kV for the 180° configuration demonstrating that considerably larger part of energy dissipated at heat at these conditions. This phenomenon can be attributed to the discharge mode conversion [32, 33]. The differences in the discharge current occur as it was shown in figure 5, where the intensity of micro discharges increases at higher voltages. It is also known that the electrode temperature influences O_3 concentration [25]. It is also clear that the electrode shape impacts gas flow hydrodynamics and therefore the

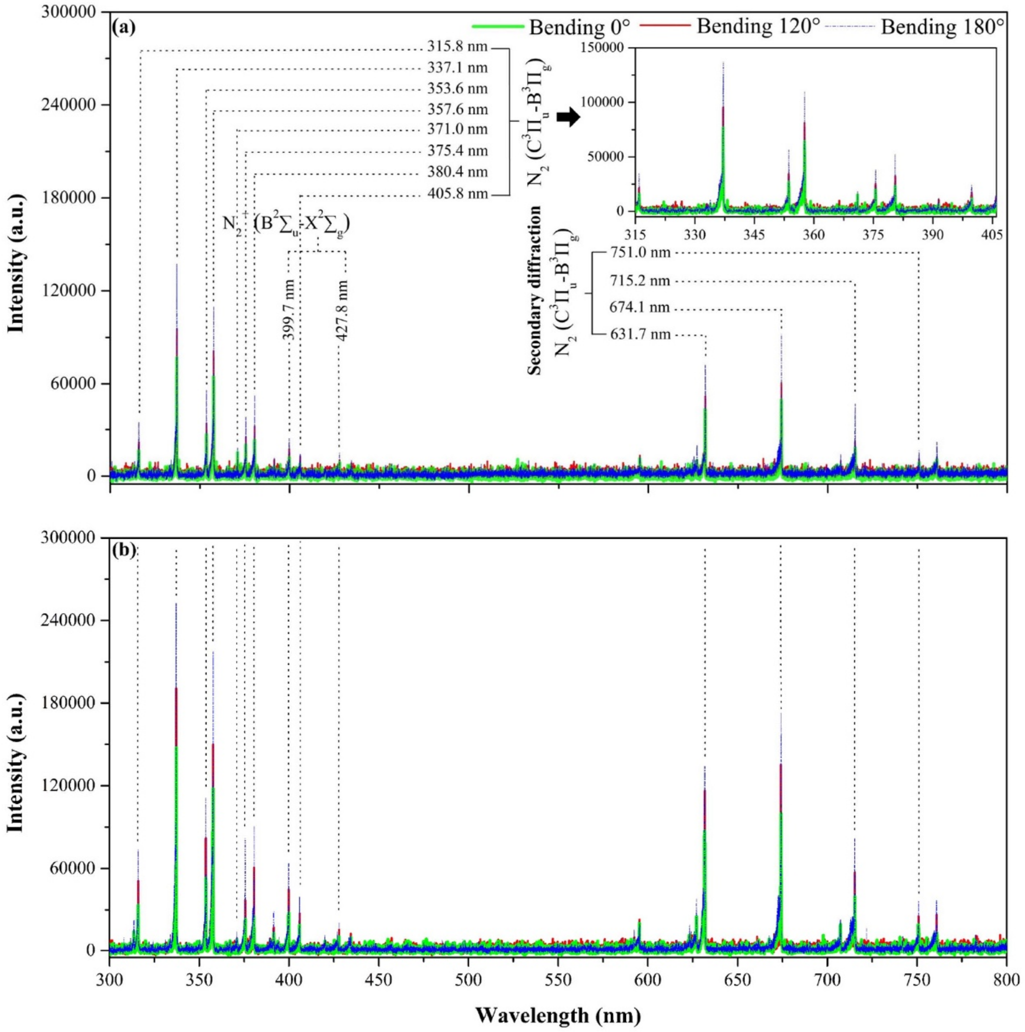

Figure 7. Optical emission spectra in the range from 300 to 800 nm from top view when the applied voltage was fixed at (a) $U_{p-p} = 4.8$ kV and (b) $U_{p-p} = 5.4$ kV.

gas residence time within the discharge region, influencing the production of reactive species [34–38].

4. Discussion

The effect of different bending configurations on the characteristic of flexible SDBD plasma collectively suggest that the bending angle has a major impact on the gas hydrodynamics around the electrode, its temperature, emission density and ozone concentration.

4.1. Production of reactive species

The key chemical reactions in air discharge plasma are listed in table 3. During a discharge, the formation of O_3 in air plasma begins from the dissociation of oxygen molecules due to electron collision to produce free oxygen atoms by $R1$ pathway. These oxygen atoms react rapidly with another O_2 molecule through $R2$ to produce O_3 [39]. There are two O_3 decomposition steps ($R3$ and $R4$), and their rates increase with temperature. Especially the $R5$ rate has a strong temperature dependence [40]. As a result, the ozone yield decreases under high temperature conditions.

Moreover, the N_2 ($C \rightarrow B$) exited state is principally generated by $N_2(C)$ transition, which is, in turn, generated by electron collision excitation of the ground state $N_2(X)$ and metastable state $N_2(A)$ by $R5$ and $R6$ pathways [41]. The nitrogen is more easily excited to the first electronic state $N_2(A)$ by electron-impact collisions at high temperature [42]. Since the 180° configuration has the maximum temperature, the $N_2(C \rightarrow B)$ density has the maximum value.

4.2. Power distribution

Many studies have shown that power consumption has a key regulating effect on the surface air discharge plasma [49, 50]. To further explore the relationship among power consumption, reactive species and electrode temperature, we use a simplified power distribution model to estimate the total power (P_{total}) as the sum of power fraction to generate light (P_1), to make ozone (P_2) and it concurrently generate heat (P_3):

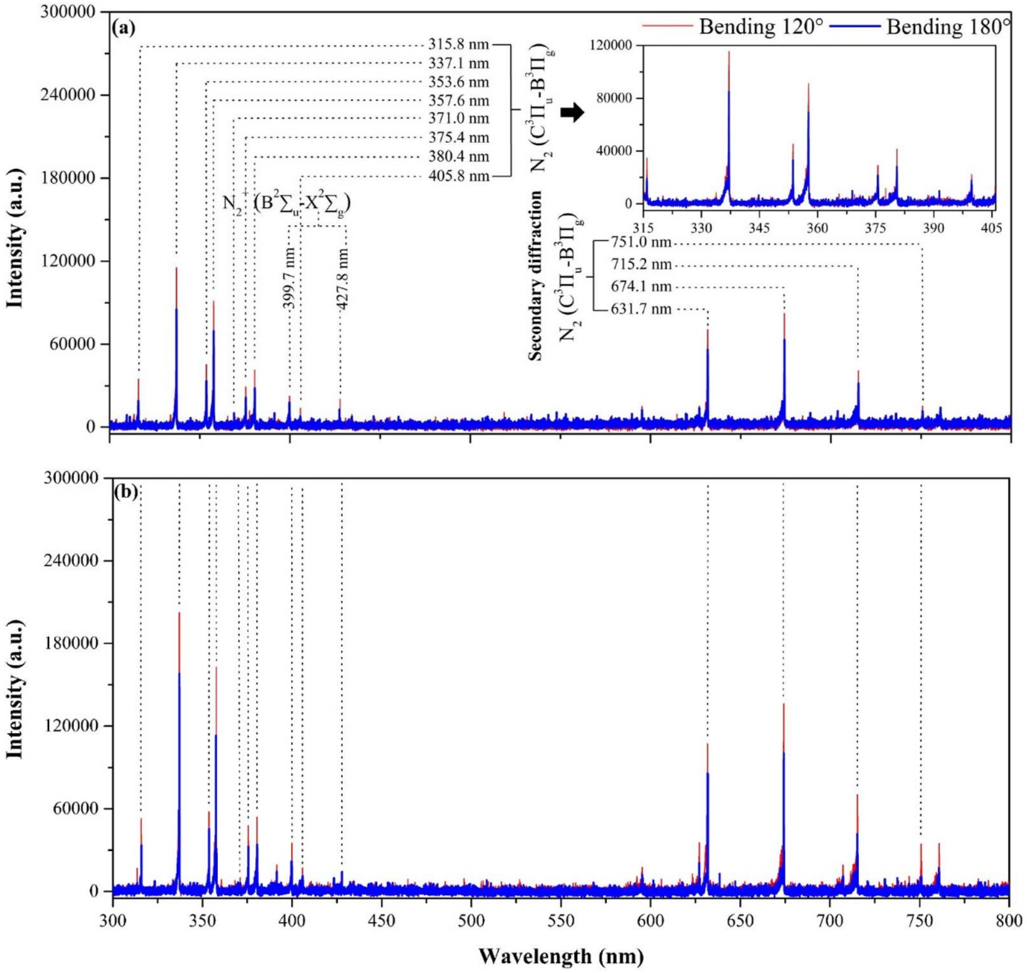

Figure 8. Optical emission spectra in the range from 300 to 800 nm from side view when the applied voltage was fixed at (c) $U_{p-p} = 4.8$ kV and (d) $U_{p-p} = 5.4$ kV.

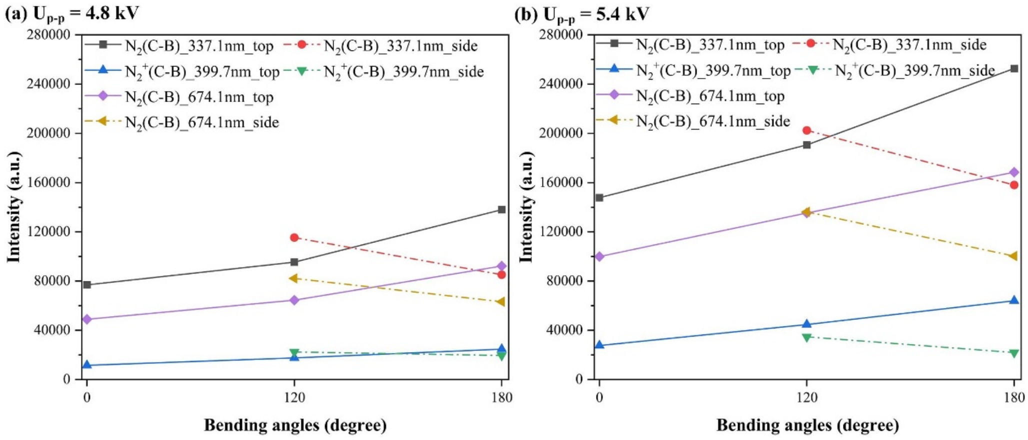

Figure 9. Emission intensity of the molecular nitrogen $N_2(C^3\Pi_u$ mi$B^3\Pi_g)$ at 337.1 nm, its secondary diffraction at 339.7 nm as well as the molecular nitrogen ion rotational bands $N_2^+(B^2\Sigma_u$ m $X^2\Sigma_g)$ at 674.1 nm as a function of bending angles at the applied voltage of (a) 4.8 kV and (b) 5.4 kV.

$$P_{\text{total}} = P_1\,(\text{light emission}) + P_2\,(\text{ozone production}) + P_3\,(\text{heat loss})\,. \tag{2}$$

Each power fraction is represented by the results in optical emission, ozone generation, and electrode temperature rise. The intensity of the line at 337.1 nm in $N_2(C^3\Pi_u$ C $B^3\Pi_g)$ bands corresponding to light emission, ozone concentration, and temperature increment are listed in table 4. The power distribution within the flex-SDBD plasma for these three dissipation pathways

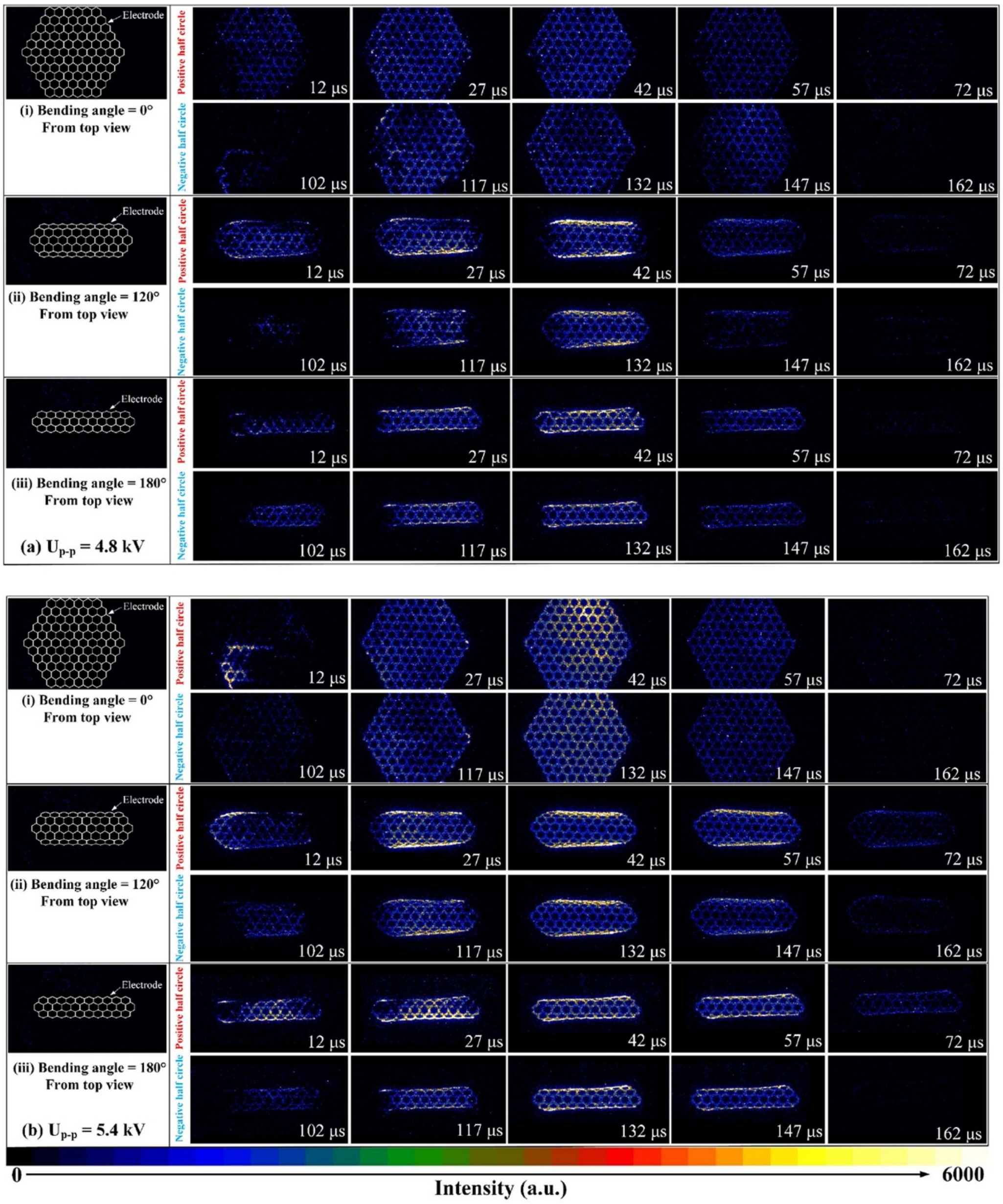

Figure 10. Top view of time-resolved images of the flex-SDBD plasma in one discharge cycle ($T = 200$ μs) at (a) 4.8 kV and (b) 5.4 kV.

was calculated relative to that observed in the 0° configuration.

The power distribution for different portions in the flex-SDBD plasma is shown in figure 14. A significant part of power dissipates as heat on the electrode, which agrees with the results by Abdelaziz *et al* [25]. The relative heat dissipation increases by 10% from 0.60 to 0.66, the power for light emission increases by 55.6% from 0.18 to 0.28 while the fraction of power towards ozone formation decreases by 45.5% from 0.22 to 0.12 with increasing bending angle at a voltage of 4.8 kV. A similar trend was also observed at 5.4 kV, while the amount of energy dissipated as heat was higher while that for light emission decreased. The power for ozone generation decreased by 28.6% from 0.21 to 0.15 with the increase of bending angle. This can be explained by the enhancement of local electric field near the bending axis due to reduced radius of curvature [47]. This, in turn, increases the light emission (figure 7), and reduces radiative and convective heat losses. Furthermore, increasing the applied voltage slightly increases the power spent for ozone generation at the expense of decreasing the emission density and sharply increasing heat generation, decreasing the energy efficiency. As it was discussed above, the discharge mode changes from corona discharge to arc discharge mode, which

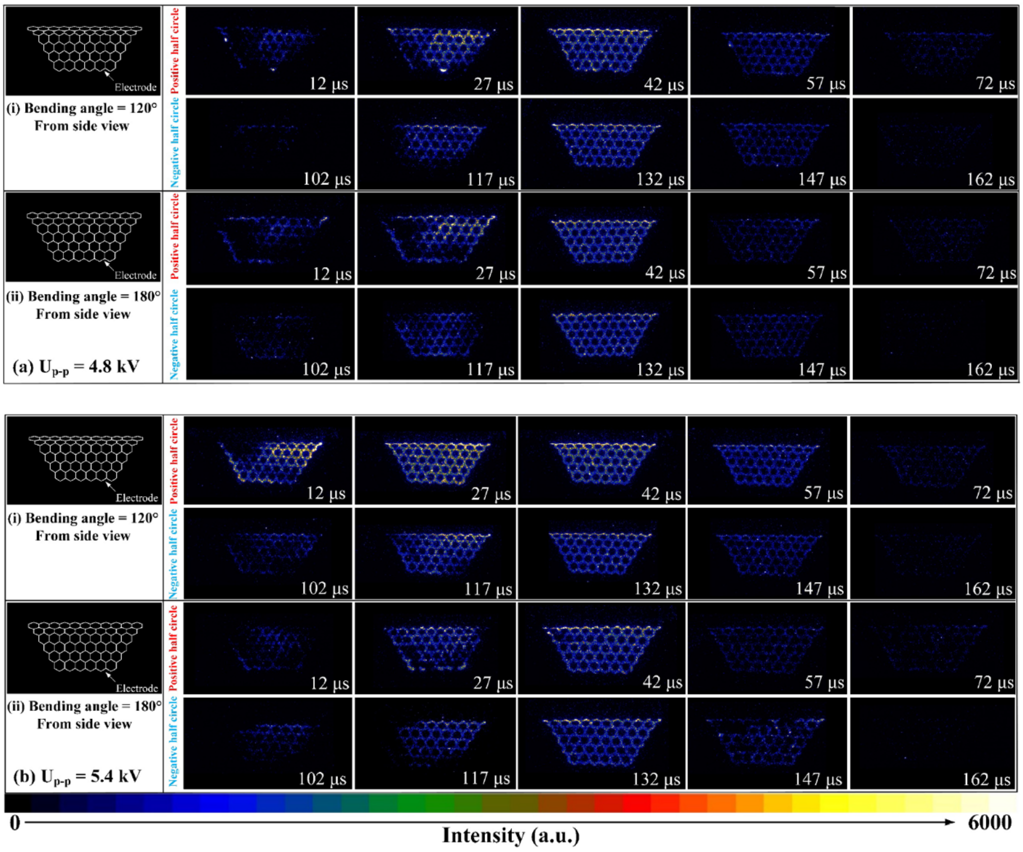

Figure 11. Side view of time-resolved images of the evolutions of the flex-SDBD plasma in one discharge cycle ($T = 200$ μs) at (a) 4.8 kV and (b) 5.4 kV.

Table 2. Mean value of light intensity in one discharge cycle.

Parameters/mean light intensity	$U_{p-p} = 4.8$ kV	$U_{p-p} = 5.4$ kV
0°—config.	261.8	480.4
120°—config. from top view	549.2	963.7
180°—config. from top view	701.5	1172.7
120°—config. from side view	421.1	659.6
180°—config. from side view	372.3	506.9

The abbreviations included in the table are as follows: 0° configuration (0°—config.), 120° configuration (0°—config.) and 180° configuration (180°—config.).

results in the higher heat dissipation above 5.4 kV [32, 33]. Thus, the bending angle significantly redistributes the power portion lost for electrode heating and used for ozone generation. A lower applied voltage is desirable for improved energy efficiency.

4.3. Equivalent circuit

The equivalent circuit of flex-DBD device is shown in figure 15. C_B and C_{BC} are the capacitance of the flex-DBD device excluding the hexagonal cavities and the solid portion, respectively. The parallel R_g and C_g are the equivalent resistor and capacitor of the open-air portion of the hexagonal cavities, respectively. C_0 is the sampling capacitor, and R_L and L are the resistance and the inductance of the secondary coil of the transformer of the power supply [19]. During operation, the total capacitance of the flex-DBD can be estimated as $C \approx C_B + C_{\mathrm{BC}}$. Considering that the bending angle will not change the total discharge area, the capacitance will almost remain the same value for these three bending angles of 0°, 120° and 180° configuration.

However, the presence of the plasma resistance R_g reflects average power used by the discharge to ionize the gas [51]. In other words, the equivalent resistance of three bending configuration is positively correlated with the average power deposited in the plasma. Since the power consumption has no significant difference between three bending configurations, the R_g values do not depend on the bending angles. In addition, for a certain reactor configuration, the value of C_B, C_{BC}, and C_g could be calculated from the reactor's geometry, the quantitative values of R_g could be further investigated.

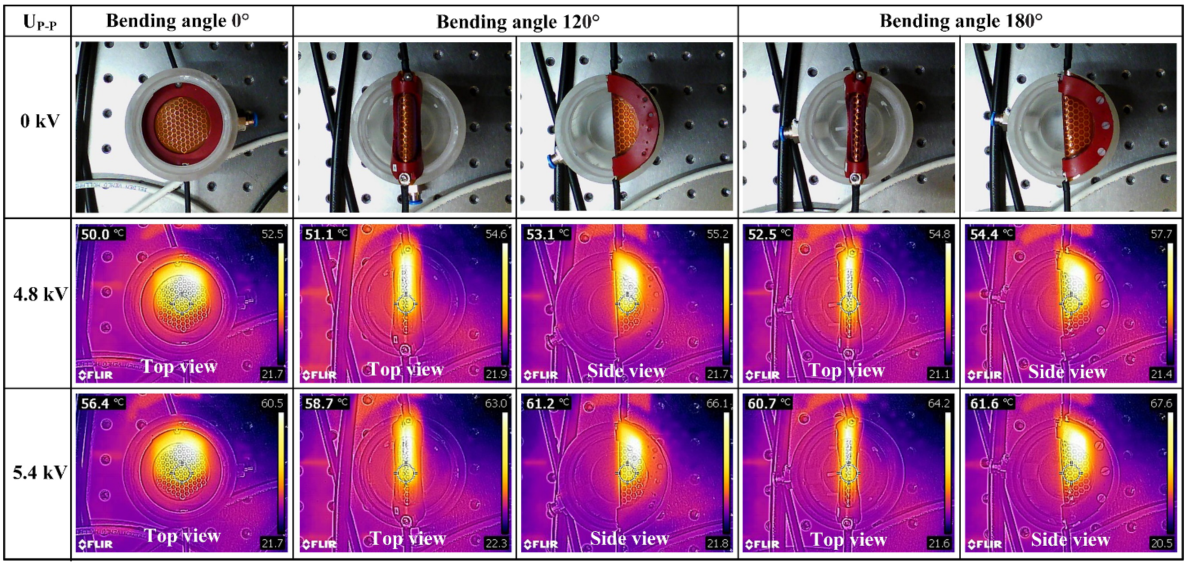

Figure 12. Thermal images of flex-SDBD plasma recorded after 60 s.

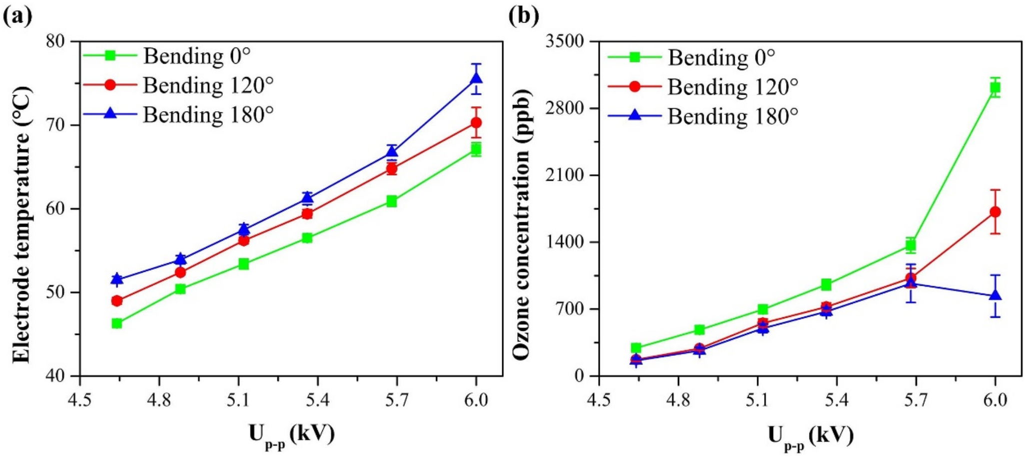

Figure 13. (a) Mean electrode temperature; (b) Mean ozone concentration as a function of applied voltage.

Table 3. Key chemical reactions in air discharge plasma.

No.	Reaction	References
R1	$e + O_2 \rightarrow e + 2O$	[43]
R2	$O + O_2 + M \rightarrow O_3 + M$	[44]
R3	$O_3 + O \rightarrow O_2 + O_2$	[45]
R4	$O_3 \rightarrow O_2 + O$	[46]
R5	$e + N_2(A) \rightarrow e + N_2(C)$	[47]
R6	$e + N_2(X) \rightarrow e + N_2(C)$	[48]

M denotes the third body species, N_2 and O_2.

In summary, the electrode bending angle has no noticeable impact on the overall power consumption and equivalent resistance, yet it plays a significant role in the power distribution between different reactive species as well as heat dissipation. The results indicated that non-bending configuration under low voltage operation is beneficial for high energy efficiency while high voltage operation favors O_3 production, which provides a promising solution for biomedical and environmental applications. In addition, to further explore the physical mechanism of flex-DBD such as filamentary discharge regime, a numerical simulation of the Laplacian field could be considered in future works.

Table 4. The power distribution in the flex-SDBD plasma.

Operation at $U_{p-p} = 4.8$ kV	Emission density	Ozone production/ppb	Temperature increment/°C	Relative power consumption
0°—config.	76 923	484	30.5	1
120°—config.	102 792	288	32.4	1.01
180°—config.	108 706	267	33.9	1.06
Operation at $U_{p-p} = 5.4$ kV	**Emission density**	**Ozone production/ppb**	**Temperature increment/°C**	**Relative power consumption**
0°—config.	137 727	956	36.5	1
120°—config.	184 554	723	39.4	1.02
180°—config.	199 704	675	41.2	1.05

The abbreviations included in the table are as follows: 0° configuration (0°—config.), 120° configuration (0°—config.) and 180° configuration (180°—config.).

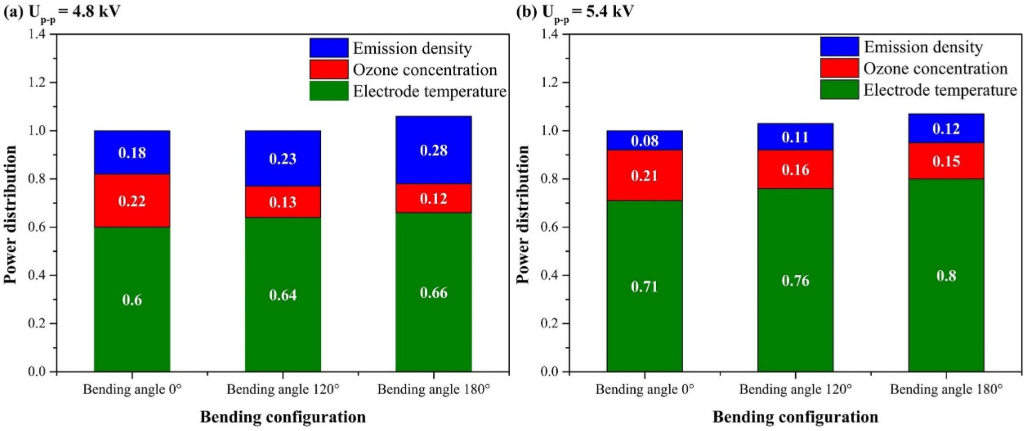

Figure 14. The power distribution for different portions in the flex-SDBD plasma when the applied voltage was fixed at (a) 4.8 kV and (b) 5.4 kV.

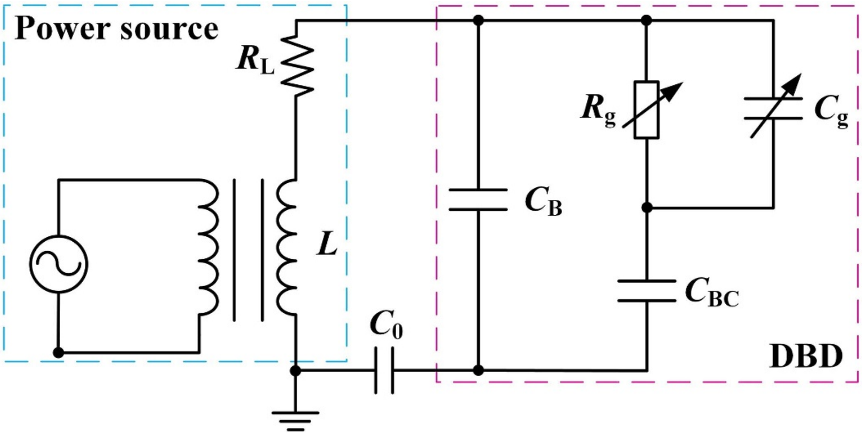

Figure 15. The equivalent circuit of flex-SDBD.

5. Conclusion

The effect of electrode deformation on the plasma discharge characteristics in an air flexible SDBD plasma powered with an AC power supply was studied. In the bending configuration, the discharge first initiates in the central part of the electrode and then propagates to the bending axis where continues luminescence is observed due to the high electrical field. The highest ozone concentration of 3.02 ppm was observed in a non-bending configuration at a voltage of 6 kV. The ozone concentration decreases with increasing the bending angle while the equivalent circuit resistance values do not depend on the bending angles. The energy efficiency towards ozone formation increases from 0.12 to 0.18 as voltage decreases to

4.8 kV. Thus, the bending angle significantly redistributes the power portion lost for electrode heating and used for ozone reduction.

Data availability statement

All data that support the findings of this study are included within the article (and any supplementary files).

Acknowledgments

Authors acknowledged funding from UK Space Agency, 'All-in-One Mars In-situ Resource Utilisation System using Non-thermal Plasma' (No. UKSAG22_ESE01);

Authors acknowledged funding from the European Research Council (ERC) under the European Union's Horizon 2020 research and innovation program (Grant Agreement No. 810182); ERC Synergy Grant SCOPE, "Surface-COnfined fast-modulated Plasma for process and Energy intensification in small molecules conversion.

Authors acknowledged funding from China Scholarship Council (No. 202006160094).

ORCID iDs

Jiayin Li https://orcid.org/0000-0002-1179-1077
Desheng Zhou https://orcid.org/0000-0001-7920-1240
Xin Tang https://orcid.org/0000-0002-5081-936X
Minkwan Kim https://orcid.org/0000-0002-6192-312X

References

[1] Lu X, Liu D, Xian Y, Nie L, Cao Y and He G 2021 Cold atmospheric-pressure air plasma jet: physics and opportunities *Phys. Plasmas* **28** 100501
[2] Liu Z C, Liu D X, Chen C, Li D, Yang A J, Rong M Z, Chen H L and Kong M G 2015 Physicochemical processes in the indirect interaction between surface air plasma and deionized water *J. Phys. D: Appl. Phys.* **48** 495201
[3] Liu Z, Xu D, Liu D, Cui Q, Cai H, Li Q, Chen H and Kong M G 2017 Production of simplex RNS and ROS by nanosecond pulse N_2/O_2 plasma jets with homogeneous shielding gas for inducing myeloma cell apoptosis *J. Phys. D: Appl. Phys.* **50** 195204
[4] Stratton G R, Bellona C L, Dai F, Holsen T M and Thagard S M 2015 Plasma-based water treatment: conception and application of a new general principle for reactor design *Chem. Eng. J.* **273** 543–50
[5] Hafeez A, Shezad N, Javed F, Fazal T, Saif Ur Rehman M and Rehman F 2021 Developing multiplexed plasma micro-reactor for ozone intensification and wastewater treatment *Chem. Eng. Process.* **162** 108337
[6] Taghvaei H, Kondeti V S S K and Bruggeman P J 2019 Decomposition of crystal violet by an atmospheric pressure RF plasma jet: the role of radicals, ozone, near-interfacial reactions and convective transport *Plasma Chem. Plasma Process.* **39** 729–49
[7] Xu H, Liu D, Wang W, Liu Z, Guo L, Rong M and Kong M G 2018 Investigation on the RONS and bactericidal effects induced by He + O_2 cold plasma jets: in open air and in an airtight chamber *Phys. Plasmas* **25** 113506
[8] Sakudo A, Yagyu Y and Onodera T 2019 Disinfection and sterilization using plasma technology: fundamentals and future perspectives for biological applications *Int. J. Mol. Sci.* **20** 5216
[9] Fridman G, Peddinghaus M, Balasubramanian M, Ayan H, Fridman A, Gutsol A and Brooks A 2006 Blood coagulation and living tissue sterilization by floating-electrode dielectric barrier discharge in air *Plasma Chem. Plasma Process.* **26** 425–42
[10] Brandenburg R 2017 Dielectric barrier discharges: progress on plasma sources and on the understanding of regimes and single filaments *Plasma Sources Sci. Technol.* **26** 053001
[11] Wu S, Cheng W, Huang G, Wu F, Liu C, Liu X, Zhang C and Lu X 2018 Positive streamer corona, single filament, transient glow, dc glow, spark, and their transitions in atmospheric air *Phys. Plasmas* **25** 123507
[12] Li J, Wu F, Xian Y, Lu X and Nie L 2022 Temporal gas temperature of atmospheric pressure air plasma *Curr. Appl. Phys.* **34** 41–49
[13] Eto H, Ono Y, Ogino A and Nagatsu M 2008 Low-temperature sterilization of wrapped materials using flexible sheet-type dielectric barrier discharge *Appl. Phys. Lett.* **93** 221502
[14] Laroussi M and Akan T 2007 Arc-free atmospheric pressure cold plasma jets: a review *Plasma Process. Polym.* **4** 777–88
[15] Jakob H, Paliwoda M, Rovey J L and Kim M 2023 Surface DBD plasma microbubble reactor for degrading methylene blue *Phys. Scr.* **98** 025603
[16] Pons J, Moreau E and Touchard G 2005 Asymmetric surface dielectric barrier discharge in air at atmospheric pressure: electrical properties and induced airflow characteristics *J. Phys. D: Appl. Phys.* **38** 3635
[17] Boekema B K H L, Vlig M, Guijt D, Hijnen K, Hofmann S, Smits P, Sobota A, van Veldhuizen E M, Bruggeman P and Middelkoop E 2015 A new flexible DBD device for treating infected wounds: in vitro and ex vivo evaluation and comparison with a RF argon plasma jet *J. Phys. D: Appl. Phys.* **49** 044001
[18] Kim D-G, Jung S and Lee S 2018 Flexible electronics technologies for the fabrication of surface dielectric barrier discharge devices *Clin. Plasma Med.* **9** 5–6
[19] Gershman S, Harreguy M B, Yatom S, Raitses Y, Efthimion P and Haspel G 2021 A low power flexible dielectric barrier discharge disinfects surfaces and improves the action of hydrogen peroxide *Sci. Rep.* **11** 4626
[20] Xie J, Chen Q, Suresh P, Roy S, White J F and Mazzeo A D 2017 Paper-based plasma sanitizers *Proc. Natl Acad. Sci.* **114** 5119–24
[21] Weltmann K-D, Fricke K, Stieber M, Brandenburg R, von Woedtke T and Schnabel U 2012 New nonthermal atmospheric-pressure plasma sources for decontamination of human extremities *IEEE Trans. Plasma Sci.* **40** 2963–9
[22] Liu B, Qi F, Zhou D, Nie L, Xian Y and Lu X 2022 A novel flexible plasma array for large-area uniform treatment of an irregular surface *Plasma Sci. Technol.* **24** 035403
[23] Kim J, Park S and Choe W 2021 Surface plasma with an inkjet-printed patterned electrode for low-temperature applications *Sci. Rep.* **11** 12206
[24] Guo Y, Fang M, Zhang L, Sun J, Wang X, Tie J, Zhou Q, Zhang L and Luo H 2022 Study on flexible surface dielectric barrier discharge plasma film for in situ inactivation of bacteria and viruses *Appl. Phys. Lett.* **121** 074101
[25] Abdelaziz A A, Ishijima T, Seto T, Osawa N, Wedaa H and Otani Y 2016 Characterization of surface dielectric barrier discharge influenced by intermediate frequency for ozone production *Plasma Sources Sci. Technol.* **25** 035012
[26] Li J, Wu F, Nie L, Lu X and Ostrikov K 2020 The production efficiency of reactive oxygen and nitrogen species (RONS)

of AC and pulse-DC plasma jet *IEEE Trans. Plasma Sci.* **48** 4204–14

[27] Fricke K, Koban I, Tresp H, Jablonowski L, Schröder K, Kramer A, Weltmann K-D, von Woedtke T and Kocher T 2012 Atmospheric pressure plasma: a high-performance tool for the efficient removal of biofilms *PLoS One* **7** e42539

[28] Zhu Z, Zhang M, Wang L, Zhang J, Luo S, Wang Z, Guo L, Liu Z, Liu D and Rong M 2023 Comparison of discharge mode transition of air plasma under pulsed and sinusoidal excitations *J. Phys. D: Appl. Phys.* **56** 355201

[29] Lu X, Fang Z, Dai D, Shao T, Liu F, Zhang C, Liu D, Nie L and Jiang C 2023 On the chronological understanding of the homogeneous dielectric barrier discharge *High Volt.* **8** 1132–50

[30] Massarczyk R, Chu P, Dugger C, Elliott S R, Rielage K and Xu W 2017 Paschen's law studies in cold gases *J. Instrum.* **12** 06019

[31] Wang W, Guo L, Yao Z, Xi W, Zhao Y, Lv J, Zhang J, Liu Z and Liu D 2022 Nitrox surface discharge used for water activation: the reactive species and their correlation to the bactericidal effect *J. Phys. D: Appl. Phys.* **55** 265203

[32] Sun Y, Zeng M and Cui Z 2012 Research on electrical characteristics of dielectric barrier discharge and dielectric barrier corona discharge *Jpn. J. Appl. Phys.* **51** 09MF15

[33] Yao J, Miao J, Li J, Lian X and Ouyang J 2023 Asymmetric discharges of dielectric barrier discharge in atmospheric air *Appl. Phys. Lett.* **122** 082905

[34] Xi W, Luo S, Liu D, Wang Z, Liu Z, Guo L, Wang X and Rong M 2022 The effect of humidity on the discharge mode transition of air discharge plasma *Phys. Plasmas* **29** 090701

[35] Yuan D, Zhang G, Ling Z, Wu A, He Y and Wang Z 2020 Characteristics of temperature distribution in atmospheric pulsed surface dielectric barrier discharge for ozone production *Vacuum* **176** 109351

[36] Wei L, Xu M and Zhang Y 2017 Energy conversion and temperature dependence in ozone generator using pulsed discharge in oxygen *Ozone* **39** 33–43

[37] Pekárek S and Mikeš J 2014 Temperature-and airflow-related effects of ozone production by surface dielectric barrier discharge in air *Eur. Phys. J.* D **68** 310

[38] Jodzis S and Baran K 2022 The influence of gas temperature on ozone generation and decomposition in ozone generator. How is ozone decomposed? *Vacuum* **195** 110647

[39] Xi W, Wang W, Liu Z, Wang Z, Guo L, Wang X, Rong M and Liu D 2020 Mode transition of air surface micro-discharge and its effect on the water activation and antibacterial activity *Plasma Sources Sci. Technol.* **29** 095013

[40] Mok Y S 2004 Oxidation of NO to NO_2 using the ozonization method for the improvement of selective catalytic reduction *J. Chem. Eng. Jpn.* **37** 1337–44

[41] Yang D-Z, Yang Y, S-Z L, Nie D-X, Zhang S and Wang W-C 2012 A homogeneous dielectric barrier discharge plasma excited by a bipolar nanosecond pulse in nitrogen and air *Plasma Sources Sci. Technol.* **21** 035004

[42] Gaens W V and Bogaerts A 2013 Kinetic modelling for an atmospheric pressure argon plasma jet in humid air *J. Phys. D: Appl. Phys.* **46** 275201

[43] Alves L L 2014 The IST-LISBON database on LXCat *J. Phys.: Conf. Ser.* **565** 012007

[44] Herron J T and Green D S 2001 Chemical kinetics database and predictive schemes for nonthermal humid air plasma chemistry. Part II. neutral species reactions *Plasma Chem. Plasma Process.* **21** 459–81

[45] Atkinson R, Baulch D L, Cox R A, Hampson R F Jr, Kerr J A and Troe J 1992 Evaluated kinetic and photochemical data for atmospheric chemistry: supplement IV. IUPAC subcommittee on gas kinetic data evaluation for atmospheric chemistry *J. Phys. Chem. Ref. Data* **21** 1125

[46] Hippler H, Rahn R and Troe J 1990 Temperature and pressure dependence of ozone formation rates in the range 1–1000 bar and 90–370 K *J. Chem. Phys.* **93** 6560–9

[47] Wang W, Liu Z, Chen J, Yao Z, Zhang H, Xi W, Liu D and Rong M 2021 Surface air discharge used for biomedicine: the positive correlation among gaseous NO_3, aqueous O_2-/ONOO$-$ and biological effects *J. Phys. D: Appl. Phys.* **54** 495201

[48] Liu Z, Wang S, Pang B, Zhang H, Gao Y, Xu D and Kong M G 2021 The impact of surface-to-volume ratio on the plasma activated water characteristics and its anticancer effect *J. Phys. D: Appl. Phys.* **54** 215203

[49] Shimizu T, Sakiyama Y, Graves D B, Zimmermann J L and Morfill G E 2012 The dynamics of ozone generation and mode transition in air surface micro-discharge plasma at atmospheric pressure *New J. Phys.* **14** 103028

[50] Pavlovich M J, Clark D S and Graves D B 2014 Quantification of air plasma chemistry for surface disinfection *Plasma Sources Sci. Technol.* **23** 065036

[51] Pipa A V and Brandenburg R 2019 The equivalent circuit approach for the electrical diagnostics of dielectric barrier discharges: the classical theory and recent developments *Atoms* **7** 14